

This is the peer reviewed version of the following article: Epifani, M. et al. *The ethylhexanoate route to metal oxide nanocrystal: synthesis of CoO nanooctahedra from Co<sup>II</sup> 2-ethylhexanoate* in European journal of inorganic chemistry (Ed. Wiley), vol. 2016, issue 24 (Aug. 2016), p. 3963-3968.

Which has been published in final form at:

DOI [10.1002/ejic.201600811](https://doi.org/10.1002/ejic.201600811)

This article may be used for non-commercial purposes in accordance with Wiley terms and conditions for use of self-archived versions.

# **The Ethylhexanoate Route to Metal Oxide Nanocrystals. Synthesis of CoO**

## **nanooctahedra from Co(II) 2-Ethylhexanoate**

Mauro Epifani<sup>a,\*</sup>, Peng-Yi Tang<sup>b,c</sup>, Aziz Genç<sup>b,d</sup>, Joan R. Morante,<sup>c</sup> Jordi Arbiol<sup>b,e</sup>, Raül Díaz<sup>f</sup>, Susanne Wicker<sup>g</sup>

<sup>a</sup>Consiglio Nazionale delle Ricerche – Istituto per la Microelettronica e Microsistemi (CNR -IMM), via Monteroni c/o Campus Universitario, I-73100, Lecce (Italy);

<sup>b</sup>Catalan Institute of Nanoscience and Nanotechnology (ICN2), CSIC and The Barcelona Institute of Science and Technology (BIST), Campus UAB, Bellaterra, 08193 Barcelona, Catalonia, Spain  
<sup>c</sup>Catalonia Institute for Energy Research (IREC), Jardins de les Dones de Negre 1, Sant Adrià del Besòs, Barcelona 08930, Catalonia, Spain

<sup>d</sup>Department of Metallurgy and Materials Engineering, Faculty of Engineering, Bartın University, 74100 Bartın, Turkey

<sup>e</sup>ICREA, Pg. Lluís Companys 23, 08010 Barcelona, Catalonia, Spain  
<sup>f</sup>Electrochemical Processes Unit, IMDEA Energy Institute, Avda. Ramón de la Sagra 3, 28935 Móstoles, Spain;

<sup>g</sup>University of Tuebingen, Institute of Physical and Theoretical Chemistry, Auf der Morgenstelle 15, 72076 Tuebingen, Germany

\*[mauro.epifani@le.imm.cnr.it](mailto:mauro.epifani@le.imm.cnr.it), phone: +39 0832 299775

## **Abstract**

CoO nanocrystals were prepared by solvothermal processing of Co 2-ethylhexanoate in oleylamine at 250 °C. The obtained products, identified as CoO by X-ray diffraction, had an octahedral shape, as seen by transmission electron microscopy, reflecting the cubic symmetry of the CoO crystallographic phase. The materials were converted to the Co<sub>3</sub>O<sub>4</sub> phase after heat-treatment at 400 °C. The nanocrystal evolution was investigated by FTIR spectroscopy. It was concluded that weak oleylamine bonding to the nanocrystal surface during the synthesis step favored exchange with 2-ethylhexanoato ligands, and that the interplay between the two ligands favored kinetic control of the growth, resulting in the finally observed octahedral morphology. The Co<sub>3</sub>O<sub>4</sub> phase obtained from the heat-treatment at 400 °C was used to process chemoresistive sensors, which were able to detect ethanol in dry and humid conditions (0 and 50 % r.h. H<sub>2</sub>O @ 25 °C) at low temperatures (100 °C).

**Keywords:** oxide nanocrystals; solvothermal processing; cobalt oxides; gas sensors.

## 1. Introduction

Carboxylate compounds like metal oleates are very well established precursors for the synthesis of metal oxide nanocrystals.<sup>[1]</sup> On the other hand, metal 2-ethylhexanoates are metalorganic compounds widely used as catalysts in many polymerization reactions,<sup>[2]</sup> but their use for the synthesis of metal oxide nanocrystals is much less exploited. Starting from the consideration that the metal-oxygen bond is already present in the 2-ethylhexanoate structure, as in metal oleates (and in other compounds like, for instance, metal nitrates<sup>[3]</sup>) we succeeded in synthesizing ZnO and SnO<sub>2</sub> nanocrystals by the decomposition of the related 2-ethylhexanoates in high-boiling amines.<sup>[4]</sup> Moreover, the same precursor was effective for the deposition of SnO<sub>2</sub> thin films.<sup>[5]</sup> Photo-decomposition of 2-ethylhexanoates has also been demonstrated to be applicable for preparing thin films<sup>[6]</sup> or nanoparticles.<sup>[7]</sup> This class of precursors hence seemed very versatile, and their presence for a large number of elements, coupled with low cost, air stability and low toxicity suggested to further explore their generality as metal oxide precursors. In fact, as stated above, there are still few works where they are exploited in such a way: these include intermetallic PtPb nanoparticles prepared by using lead(II) 2-ethylhexanoate,<sup>[8]</sup> CeO<sub>2</sub> and SnO<sub>2</sub> self-capped nanocrystals,<sup>[9]</sup> MoO<sub>3</sub> nanoparticles,<sup>[10]</sup> colloidal In-doped ZnO nanocrystals,<sup>[11]</sup> kersterite nanocrystals.<sup>[12]</sup> Extending this class of precursors, then, is of interest for the many underlined practical advantages, but also from a fundamental point of view, for enlarging the body of knowledge related to nanochemistry precursors. In this work, we show the successful synthesis of CoO nanooctahedra by decomposition of Co 2-ethylhexanoate in oleylamine. The phase stability of the nanostructures was also investigated, showing that at 400 °C phase transformation to Co<sub>3</sub>O<sub>4</sub> took place. Moreover, both CoO and Co<sub>3</sub>O<sub>4</sub> are of remarkable interest for their fundamental physical properties and for many applications related, for instance, to energy storage<sup>[13]</sup>. In this sense, it is of further interest the availability of readily synthesized nanocrystals, with a simple and low temperature procedure that extends the range of existing approaches like molten salt<sup>[14]</sup>, and combustion synthesis, together with

other colloidal syntheses discussed below. The resulting materials were used for processing gas-sensing devices.

## 2. Materials and methods

In a typical synthesis, 1 g of Co 2-ethylhexanoate (65% in mineral spirits, Strem Chemicals. In the following it will be denoted as CoEtEs<sub>2</sub>) was dissolved into 10 mL of *n*-oleylamine (OAm, 70%, Sigma-Aldrich) in a 16 ml glass vial. Then the vial was placed into a 45 mL steel autoclave (Parr), and the autoclave heated up to 250 °C into a muffle furnace, at a rate of 5 °C/min, and kept for 2 h at such temperature. After cooling, the product was extracted with methanol, washed with acetone and dried at 90 °C. A dark-brownish powder was obtained (this sample in the following will be referred to as “dried” or “as-prepared”). The powders were heat-treated at 400 °C for 1 h in air atmosphere for thermal and phase stabilization before sensing device processing. Samples were also heat-treated at 105 °C and 305 °C for 15 min, for investigating the sample evolution during the thermal treatment.

X-ray diffraction (XRD) was carried out with a Panalytical X’Pert PRO-MPD diffractometer working with the Cu K $\alpha$  radiation ( $\lambda= 1.5406\text{\AA}$ ) using a Bragg-Brentano geometry. Rietveld refinement of the XRD patterns was carried out with the Maud software.<sup>[15]</sup>

Fourier Transform Infrared (FTIR) measurements were carried out with a Nicolet 6700 spectrometer in diffuse reflectance setup, after dispersing the sample powders in KBr.

Thermal analyses were carried out in a thermal balance model SDT Q-600 from TA instruments under air flow of 100 mL/min and thermal ramp of 10 °C/min.

High resolution transmission electron microscopy (HRTEM) analyses of the powders were carried out with a field emission gun microscope FEI Tecnai F20, working at 200 keV with a point-to-point resolution of 0.19 nm. Scanning transmission electron microscopy (STEM) in annular dark field (ADF) mode combined with electron energy loss spectroscopy (EELS) spectrum imaging (SI) were also obtained in the same FEI Tecnai F20.

Brunauer–Emmett–Teller (BET) single point specific surface area measurement on the sample heated in air at 400 °C was performed with an Autochem II 2920 Micrometrics, equipped with a TCD detector. Before measurement the sample was outgassed at 300 °C for 2 h under He flow.

The gas-sensing device was prepared out of the 400 °C pre-heated powder. A suspension of this powder and isopropanol was drop-coated onto an alumina substrate (25.4 mm × 4.2 mm × 0.6 mm), which was provided with interdigitated Pt-electrodes for resistance read-out on the front side and a Pt-heater for temperature control on the back side. During the drop-coating process the substrate was placed on a hot plate and heated to about 60 °C. Afterwards it was annealed in a four zone moving belt oven at 400 °C. The gas sensing tests were done by measuring the resistance changes of the obtained gas sensor with a Keithley 199 multimeter in operando at different temperatures 100-200 °C. For supplying different concentrations of CH<sub>4</sub> (500, 1000, and 2000 ppm), CO (20, 50, and 100 ppm), and EtOH (45, 90, and 170 ppm) in both dry and humid background conditions (0 and 50 % r.h. H<sub>2</sub>O @ 25 °C) a computer controlled gas mixing system, equipped with mass flow controllers and data acquisition cards was used. The sensor response was defined as  $R_{\text{gas}}-R_0/R_0$ , where  $R_0$  was the sensor baseline electrical resistance in synthetic air and  $R_{\text{gas}}$  indicated the sensor electrical resistance after equilibration in the target gas.

### 3. Results and Discussion

The as-prepared synthesis product was first analyzed by XRD. The related pattern is shown in **Figure 1**, where only the reflections of CoO in the cubic crystallographic phase were found (JCPDS card 43-1004). In particular, the intensity ratio between the (111) and (200) peaks was inverted with respect to the expected trend, indicating preferential growth of CoO, as confirmed by the TEM results below. Of course, similar intensity enhancement was observed for the (222) reflection at about 77.5°. No other phases were detected, demonstrating the purity of the as-prepared samples. After heat-treatment at 400 °C, the CoO phase was completely converted to the Co<sub>3</sub>O<sub>4</sub> spinel phase (JCPDS card 98-002-6720), in agreement with the known stability trends of cobalt oxide phases in air.

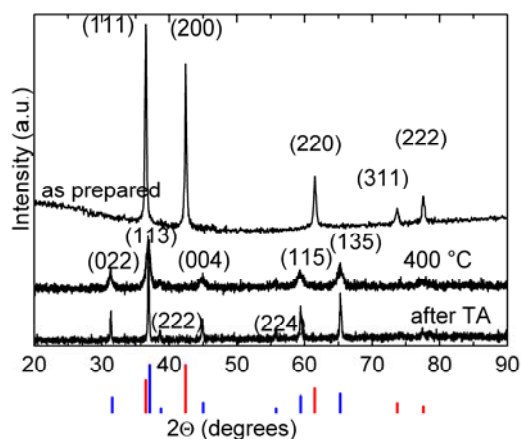


**Figure 1:** XRD patterns of the nanocrystals obtained in the indicated conditions. TA indicates the material collected after cooling from 900 °C during the thermal analyses. The theoretical intensities from CoO (red lines) and Co<sub>3</sub>O<sub>4</sub> (blue) JCPDS cards are also reported.

Similar heat-treatment in argon preserved the CoO phase (see Supporting Information). The *a* lattice parameter of the rocksalt cubic structure of the as-prepared CoO sample was 4.2598(1) Å. The *a* lattice parameter of the spinel cubic structure of Co<sub>3</sub>O<sub>4</sub> after heat-treatment at 400 °C was 8.095(2) Å. These results are in very good agreement with those reported by other groups.<sup>[16]</sup>

The structure and morphology of the as-prepared CoO nanocrystals were investigated by HRTEM and ADF STEM combined with EELS SI. **Figure 2** shows the elemental composition measured by EELS on the nanocrystals evidenced in the right part of the figure. The found atomic concentration values were 47% for Co and 53% for O, indeed confirming the CoO stoichiometry. Apparent oxygen excess is in agreement with the *p*-type semiconductor nature of CoO. Moreover, homogeneous distribution of both elements was clearly observed. Further HRTEM analyses, of which an example is reported in **Figure 3**, confirmed the  $Fm\bar{3}m$  space group of the CoO nanoparticles.

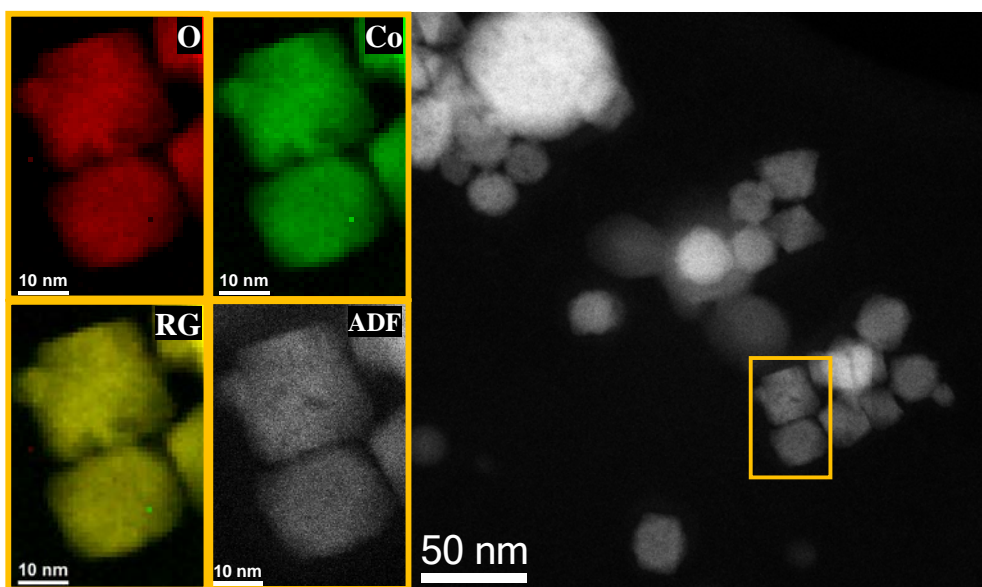


**Figure 2:** (right) ADF STEM micrograph showing typical octahedral as-prepared CoO nanoparticles on different projections. (left) EELS elemental maps for Co, O, combined RGB map and corresponding ADF STEM detail, obtained on the selected nanoparticles in the yellow squared region shown in the general view ADF STEM image on the right.

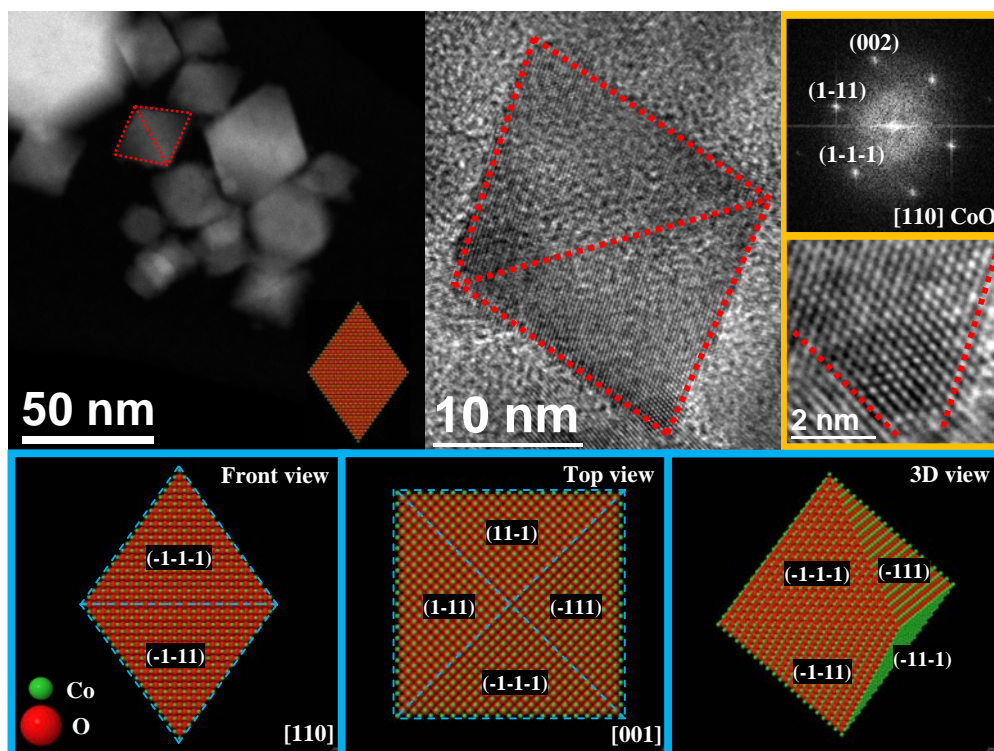


**Figure 3:** (top left) ADF STEM general view showing typical as-prepared CoO octahedral nanoparticles on different projections. The selected nanoparticle delimited with red pointed lines has been modeled in the inset. (top middle) HRTEM micrograph showing the projected facets of the octahedral CoO nanoparticle along the [110] zone axis. (top right) Power spectrum obtained on the previous HRTEM micrograph showing the cubic structure of the CoO nanoparticle along the [110] projection. The HRTEM below the power spectra shows an atomic resolution detail of the lateral facets of the octahedra corresponding to 111 planes. (bottom) Front ([110] projection), top ([001] projection) and 3D views of the octahedral nanoparticle model on the left, middle and right insets, respectively.

Combined HAADF STEM and HRTEM studies helped us to model the 3D atomic morphology of the nanoparticles. In fact every observed nanoparticle had an octahedral morphology defined by 8 (111) facets, as shown in the 3D atomic models on the bottom of the figure. 3D atomic models of the nanoparticles were constructed using the Rhodius software<sup>[17]</sup>, which has been demonstrated to be very successful in the modeling of complex nanostructures<sup>[18]</sup>. These results are in agreement with the peak intensity ratios observed in the XRD pattern of **Figure 1**.

It is remarkable the effect of the heat-treatment at 400 °C on the starting CoO nanocrystals. As discussed below, this temperature was sufficient for OAm removal, so aggregation of the nanoparticles was expected. Moreover, the stoichiometry change and the remarkable lattice parameter increase (almost doubled) due to the phase transformation to Co<sub>3</sub>O<sub>4</sub>, shown in **Figure 1**, imposed extensive reconstruction of the nanocrystals. In **Figure 4** a representative image is shown, demonstrating the phase transformation to Co<sub>3</sub>O<sub>4</sub>. In the Supporting Information another image is shown where the Co<sub>3</sub>O<sub>4</sub> nanoparticles seem to be related to cubic regions during the transformation process. It is also to be noted the smaller size with respect to the previous nanooctahedra. In fact, Rietveld refinement provided a mean size of about 35 nm, about half than that resulting from refinement of the as-prepared CoO sample.

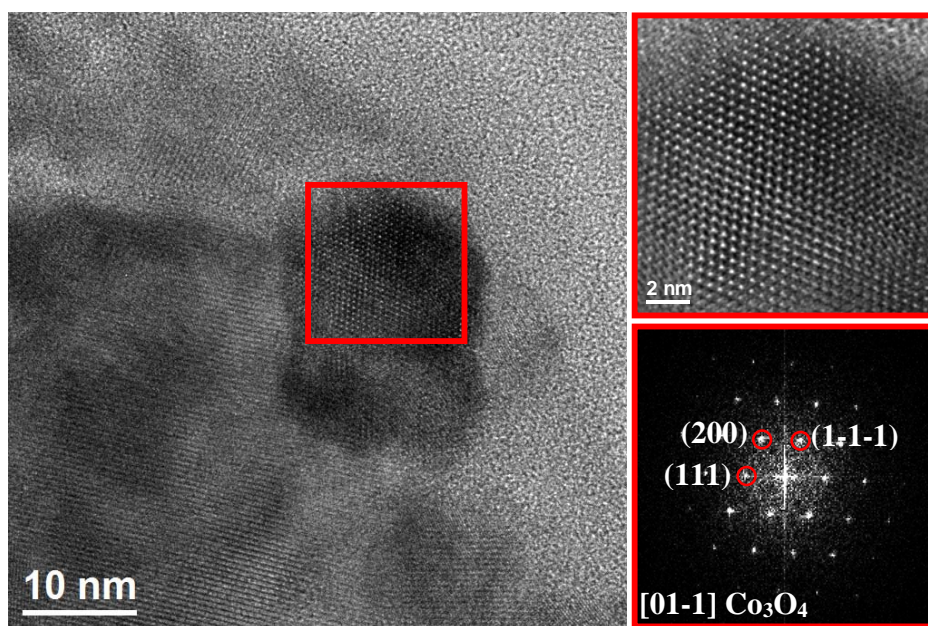


**Figure 4:** Left panel: general HRTEM micrograph of the CoO sample heat-treated at 400 °C. Right panel: the detail structure of red squared area is presented in the magnified TEM (left); the corresponding FFT spectrum (bottom) reveals these nanoparticles can be indexed to cubic (spinel)  $\text{Co}_3\text{O}_4$ , as visualized along the [01-1] direction.

This reconstruction process was probably responsible for the appreciable specific surface area of the sample which, despite the 400 °C treatment, was 49  $\text{m}^2/\text{g}$  by BET. This value well compares with 29  $\text{m}^2/\text{g}$  obtained by urea combustion method,<sup>[16]</sup> 65  $\text{m}^2/\text{g}$  by complex decomposition,<sup>[19]</sup> 82  $\text{m}^2/\text{g}$  by spray pyrolysis<sup>[20]</sup>, just to name a few. Only  $\text{Co}_3\text{O}_4$  nanorods, but prepared at lower temperature (300 °C) displayed much higher area (232  $\text{m}^2/\text{g}$ ).<sup>[21]</sup> The focus on the phase stability of the nanoparticles was necessary since sensing devices, which were the initial application aim, need high temperature pre-treatment for chemical, thermal and electrical stabilization before being operated. In particular, any organic residual should be removed from the sample. For this reason, DSC/TG measurements were carried out for selecting the proper heat-treatment temperature which, as shown above, resulted to be 400 °C.

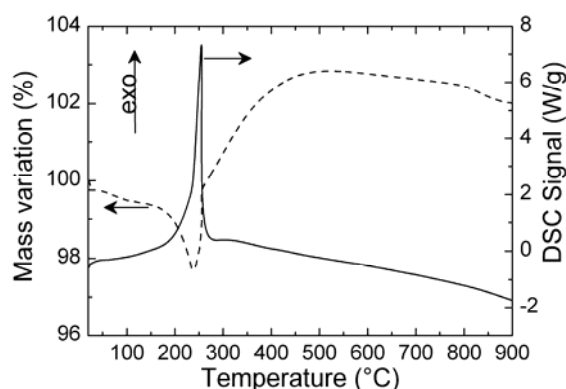


**Figure 5:** DSC/TG curves measured onto the as-prepared CoO sample.

The results are shown in **Figure 5**. The data are dominated by two main phenomena: an intense exothermic peak associated with sharp mass loss, centered at about 250 °C and that comprises a shoulder on the lower temperature flank, and a subsequent mass increase not associated with DSC peaks. The 250 °C peak was interpreted in terms of dissociation/oxidation of the oleylamine ligands bonded to the CoO nanocrystals, as shown by the FTIR data presented below. The subsequent mass increase suggested oxygen uptake from the atmosphere to form  $\text{Co}_3\text{O}_4$ , which is coherent with the sample mass surpassing the initial value. The involved temperature range is in agreement with the results of **Figure 1**. Slight mass decrease in the higher temperature range could be due to sample structural rearrangement. Bulk  $\text{Co}_3\text{O}_4$  will convert to CoO only above 950 °C. In fact, the sample collected after thermal analysis displayed the  $\text{Co}_3\text{O}_4$  XRD pattern (**Figure 1**), with remarkable peak narrowing due to the high temperature sintering. It is interesting to observe that the sample heated at 900 °C, as observed by SEM (see the Supporting Information), displayed some structures again resembling the cubic structure of CoO, despite at a much larger size imposed by high temperature.

The sample evolution could be confirmed by FTIR investigation, which also provided further insight in the material formation pathways. The spectra recorded in various steps of the synthesis process are reported in **Figure 6**, together with those of  $\text{Co}(\text{EtEs})_2$  and OAm.

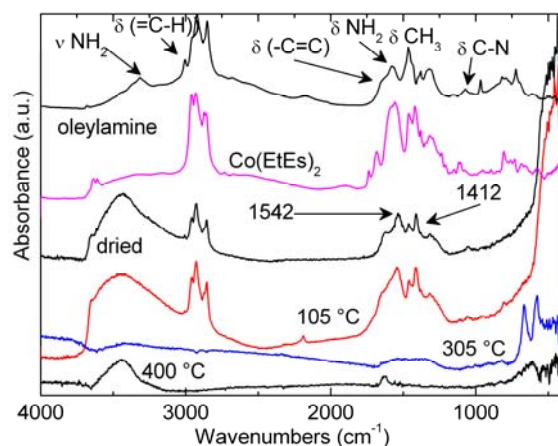


**Figure 6:** FTIR spectra measured onto the indicated samples.

In the dried CoO nanocrystals, it is possible first of all to observe an intense and broad band below  $3500\text{ cm}^{-1}$ , with a structure typical of the overlap of several OH moieties. Since the synthesis is nonaqueous, it could be speculated that the nanocrystal formation proceeds through the condensation of Co-OH bonds, but the reaction between OAm and the  $\text{Co}(\text{EtEs})_2$  will require specific investigation for being identified. It will be worth mentioning that reaction with oleic acid only provided a small amount of a waxy material. More interestingly, the investigation of the sample composition offers hints about synergistic effect of OAm and 2-ethylhexanoto ligands in the synthesis of the final CoO nanocrystals. OAm has been used in reaction with  $\text{Co}(\text{acac})_3$ <sup>[22]</sup> in two different works, yielding CoO but without the clear shape obtained in the present work. Different shapes were obtained by the decomposition of cobalt oleate in presence of oleic acid.<sup>[23]</sup> Cobalt acetate decomposition in OAm only provided elemental Co nanocrystals, while large CoO octahedral were obtained in a mixture of OAm and oleic acid. In this case, the role of OAm was recognized as that of a reducing agent. Decomposition of  $\text{Co}(\text{acac})_2$  required a mixture of oleic acid, OAm and cethyltrimethylammonium bromide for getting octahedral nanocrystals. In earlier studies, decomposition of  $\text{Co}(\text{acac})_3$  in oleylamine had been used, with different shapes of the final CoO nanocrystals.<sup>[24]</sup> Coming to the present study, in the as-prepared sample the  $\nu$  ( $\text{NH}_2$ ) at about  $3300\text{ cm}^{-1}$  is hidden by the OH signal, but the presence of OAm is nevertheless ensured

by a very weak  $\delta$  (C-H) signal at  $3004\text{ cm}^{-1}$ , the  $\delta$ (-C=C) band at about  $1645\text{ cm}^{-1}$  (the Co precursor does not have any band in that region) and further  $\delta$  (NH<sub>2</sub>) and  $\delta$  (C-N) persistence. The  $\delta$  (CH<sub>3</sub>) band at about  $1465\text{ cm}^{-1}$  is not indicative since it receives a contribution even from any 2-ethylhexanoate residual. On the other hand, the OAm signal is quite weak, and suggests that its bonding to the CoO surface is not strong enough to survive the washing steps. In fact, the mass loss in the thermal analysis associated with oleylamine desorption (about 2%, see **Figure 5**) was very limited. An important feature is a couple of new bands at about  $1542$  and  $1412\text{ cm}^{-1}$ . These bands, due to asymmetric and symmetric carboxylate stretching modes, respectively, are typical of the coordination of a carboxylic acid to a metal ion.<sup>[25]</sup> They are accompanied by the disappearance of the carbonyl band of the free acid at about  $1740\text{ cm}^{-1}$ . In fact, the spectrum of the Co precursor contained a band at  $1740\text{ cm}^{-1}$  which was no more observed in the dried sample. Moreover, in the 2-ethylhexanoate molecule itself, we already had the carboxylate ions. From the  $130\text{ cm}^{-1}$  value of  $\Delta$ , the separation between the carboxylate stretching modes, we can deduce that the bonding is of chelating type.<sup>[25-26]</sup> Summarizing: The CoO surface is coordinated with OAm and 2-ethylhexanoato moieties, the latter in chelating configuration, but the OAm bonding to the nanocrystal surface is weak and can be easily substituted, during the growth, by the 2-ethylhexanoato ligands generated by Co(EtEs)<sub>2</sub>. The dynamic interplay between the two ligands originates the peculiar shape of the nanocrystals. By “peculiar” we do not mean that it is an unexpected shape, being closely related to the crystal symmetry of CoO, but that the combination of the two ligands is tuned in such a way to provide the proper kinetic control over the growth, allowing such stable crystallographic habit to emerge. The spectra for  $105\text{ }^{\circ}\text{C}$  and  $305\text{ }^{\circ}\text{C}$ , soon before and after the intense exothermic peak discussed in **Figure 5**, confirm the interpretation of the thermal analysis data. After heating at  $105\text{ }^{\circ}\text{C}$ , the IR signal is identical to the as-prepared sample, since the exothermic phenomena have not begun yet. Instead, at  $305\text{ }^{\circ}\text{C}$ , after the peak completion, the IR signal drastically changed in the region characterized by OAm and 2-ethylhexanoate modes. This result confirms that the exothermic peak was due to organics desorption/decomposition. It will be noted that the intense peaks around  $1500$

$\text{cm}^{-1}$  were substituted by broad and weak bands, showing that some species are still present. They could be partly responsible for the slightly mass decrease at high temperatures observed in **Figure 5**. After 400 °C, no signals were observed apart for OH, water and typical oxide modes at low wavenumbers, indicating complete thermal and chemical stabilization of the material.

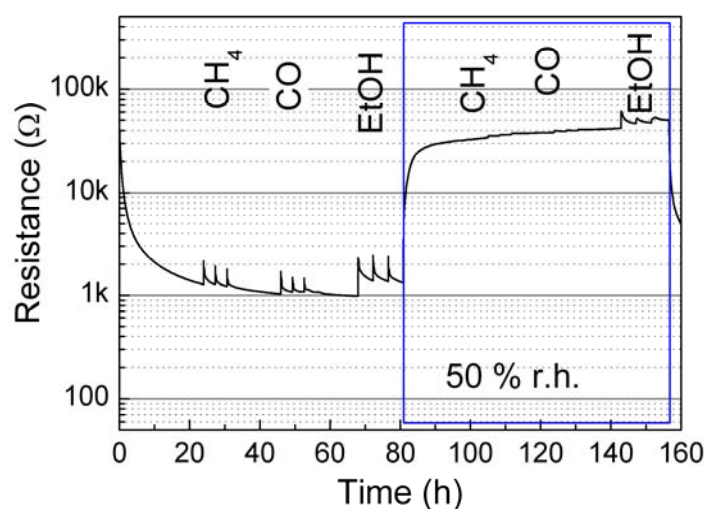


**Figure 7:** Resistance measurement of  $\text{Co}_3\text{O}_4$  sensor at 100 °C under  $\text{CH}_4$  (500, 1000, and 2000 ppm), CO (20, 50, and 100 ppm), and EtOH (45, 90, and 170 ppm) exposure in dry and humid synthetic air background (0 and 50 % r.h.  $\text{H}_2\text{O}$  @ 25 °C).

The gas sensing properties of the prepared sensor was evaluated towards three different gases ( $\text{CH}_4$ , CO, and EtOH). The raw resistance data of the measurement are plotted in Figure 7, showing typical p-type behavior through resistance increase during exposure to reducing gases. The corresponding response data are reported in **Table 1**. It can be seen, that the  $\text{Co}_3\text{O}_4$ -sensor responses to all three gases in dry conditions, but is rather selective to ethanol in humidity (50 % r.h.  $\text{H}_2\text{O}$  @ 25 °C). In general, the highest response was obtained to this gas. If we focus onto ethanol sensing, the response data are not comparable with those recently reported.<sup>[27]</sup> They are more comparable but still smaller than that obtained with various  $\text{Co}_3\text{O}_4$  morphologies,<sup>[27b, 28]</sup> The comparison is more useful is the related operating temperatures are considered. While in literature they are easily higher than 200 °C<sup>[29]</sup> and up to 300 °C,<sup>[30]</sup> in our case the highest response was observed at 100 °C and not at higher temperatures, indicating

that the  $\text{Co}_3\text{O}_4$  prepared by this procedure is suitable for low temperature gas detection. This result compensates the relatively low responses obtained. The lowered response to  $\text{CH}_4$  and  $\text{CO}$  in humid air indicates that these gases are competing with  $\text{H}_2\text{O}$  for the same adsorption sites more than  $\text{EtOH}$ .

**Table 1:** Response data at operating temperature of  $100\text{ }^\circ\text{C}$  calculated from the curves in Figure 7

Test Gas		Response		Response		Response
$\text{CH}_4$	<i>ppm</i>	500		1000		2000
	r.h. 0 %	1.7		1.5		1.4
	r.h. 50 %	1.0		1.0		1.0
$\text{CO}$	<i>ppm</i>	20		50		100
	r.h. 0 %	1.5		1.4		1.4
	r.h. 50 %	1.0		1.0		1.0
$\text{EtOH}$	<i>ppm</i>	45		90		170
	r.h. 0 %	2.4		2.3		2.4
	r.h. 50 %	1.5		1.2		1.3

#### 4. Conclusions

It is possible to extend the applicability of metal 2-ethylhexanoates as precursors for the synthesis of metal oxide nanostructures. Cobalt 2-ethylhexanoate is in fact a convenient precursor for the synthesis of  $\text{CoO}$  nanostructures, likely through the reaction of oleylamine with 2-ethylhexanoate ligands. The resulting nanocrystals have the shape of nanooctahedra, related with the crystal phase of  $\text{CoO}$ , and are converted to  $\text{Co}_3\text{O}_4$  upon high temperature treatment, in agreement with the analogous phase transformations of bulk  $\text{CoO}$ . The resulting materials are suitable for processing low temperature chemical gas sensors.

#### 5. Acknowledgements

Authors acknowledge the SOLAR project (DM19447). We thank Fernando Pico for the XRD measurements, Giovanni Battista Pace for the help with the sample preparation, Teresa Andreu and Marta M. Natile for additional characterizations. Funding from Generalitat de Catalunya 2014 SGR 1638 and the Spanish MINECO coordinated projects between IREC and ICN2 TNT-FUELS and e-TNT (MAT2014-59961-C2-2-R) and the Severo Ochoa Excellence Program. Part of the present work has been performed in the framework of Universitat Autònoma de Barcelona Materials Science PhD program.

## References

- [1] Y. W. Jun, J. S. Choi, J. Cheon, *Angew. Chem. Int. Ed.* **2006**, *45*, 3414-3439.
- [2] a) N. N. Glebova, N. N. Kostitsyna, O. K. Sharaev, V. A. Yakovlev, *Polym. Sci. Ser. B* **2006**, *48*, 237-239; b) C. M. Kuo, S. J. Clarson, *J. Inorg. Organomet. Polym. Mater.* **2012**, *22*, 577-587; c) H. Lee, S. Do, S. Lee, H. Kim, C. Bae, S. Jung, B. Y. Lee, G. Kwag, *Polymer* **2014**, *55*, 6483-6487; d) Z. M. Li, G. P. Yan, C. W. Ai, Q. Zhang, L. Li, F. Liu, X. H. Yu, B. A. Zhao, *J. Appl. Polym. Sci.* **2012**, *124*, 3704-3713; e) T. Sadik, V. Massardier, F. Becquart, M. Taha, *Polymer* **2012**, *53*, 4585-4594; f) M. Winkler, T. M. Lacerda, F. Mack, M. A. R. Meier, *Macromolecules* **2015**, *48*, 1398-1403.
- [3] D. S. Wang, T. Xie, Q. Peng, S. Y. Zhang, J. Chen, Y. D. Li, *Chem. Eur. J.* **2008**, *14*, 2507-2513.
- [4] M. Epifani, J. Arbiol, R. Diaz, M. J. Peralvarez, P. Siciliano, J. R. Morante, *Chem. Mater.* **2005**, *17*, 6468-6472.
- [5] M. Epifani, L. Francioso, P. Siciliano, A. Helwig, G. Mueller, R. Diaz, J. Arbiol, J. R. Morante, *Sens. Actuators, B* **2007**, *124*, 217-226.
- [6] a) L. S. Andronic, R. H. Hill, *J. Photochem. Photobiol., A* **2002**, *152*, 259-265; b) H. H. Park, X. Zhang, S. W. Lee, D. J. Jeong, S. M. Lee, K. D. Kim, D. G. Choi, J. H. Choi, J. Lee, E. S. Lee, H. K. Kang, H. H. Park, R. H. Hill, J. H. Jeong, *Microelectron. Eng.* **2011**, *88*, 923-928; c) H. H. Park, X. Zhang, S. W. Lee, K. D. Kim, D. G. Choi, J. H. Choi, J. Y. Lee, E. S. Lee, H. H. Park,

- R. H. Hill, J. H. Jeong, *J. Mater. Chem.* **2011**, *21*, 657-662; d) S. Trudel, G. Z. Li, X. Zhang, R. H. Hill, *J. Photopolym. Sci. Technol.* **2006**, *19*, 467-475; e) H. J. Zhu, R. H. Hill, *J. Non-Cryst. Solids* **2002**, *311*, 174-184.
- [7] R. J. de Oliveira, P. Brown, G. B. Correia, S. E. Rogers, R. Heenan, I. Grillo, A. Galembeck, J. Eastoe, *Langmuir* **2011**, *27*, 9277-9284.
- [8] L. R. Alden, D. K. Han, F. Matsumoto, H. D. Abruna, F. J. DiSalvo, *Chem. Mater.* **2006**, *18*, 5591-5596.
- [9] Y. J. Kim, Y. S. Kim, S. Y. Chai, D. H. Cha, Y. S. Choi, W. I. Lee, *New J. Chem.* **2007**, *31*, 260-264.
- [10] E. D. Santos, F. A. Sigoli, I. O. Mazali, *J. Solid State Chem.* **2012**, *190*, 80-84.
- [11] X. Y. Liang, Y. P. Ren, S. Bai, N. Zhang, X. L. Dai, X. Wang, H. P. He, C. H. Jin, Z. Z. Ye, Q. Chen, L. W. Chen, J. P. Wang, Y. Z. Jin, *Chem. Mater.* **2014**, *26*, 5169-5178.
- [12] G. Gabka, P. Bujak, M. Gryszel, A. Ostrowski, K. Malinowska, G. Z. Zukowska, F. Agnese, A. Pron, P. Reiss, *Chem. Commun.* **2015**, *51*, 12985-12988.
- [13] a) M. V. Reddy, G. V. Subba Rao, B. V. R. Chowdari, *Chem. Rev.* **2013**, *113*, 5364-5457; b) H. Guan, X. Wang, H. Q. Li, C. Y. Zhi, T. Y. Zhai, Y. Bando, D. Golberg, *Chem. Commun.* **2012**, *48*, 4878-4880.
- [14] a) M. V. Reddy, Z. Beichen, K. P. Loh, B. V. R. Chowdari, *CrystEngComm* **2013**, *15*, 3568-3574; b) M. V. Reddy, Z. Beichen, L. J. e. Nicholette, Z. Kaimeng, B. V. R. Chowdari, *Electrochem. Solid-State Lett.* **2011**, *14*, A79-A82.
- [15] L. Lutterotti, **2011**.
- [16] M. V. Reddy, G. Prithvi, K. P. Loh, B. V. Chowdari, *ACS Appl. Mater. Interfaces* **2014**, *6*, 680-690.
- [17] S. Bernal, F. J. Botana, J. J. Calvino, C. Lopez-Cartes, J. A. Perez-Omil, J. M. Rodriguez-Izquierdo, *Ultramicroscopy* **1998**, *72*, 135-164.

- [18] a) R. R. Zamani, M. Ibáñez, M. Luysberg, N. García-Castelló, L. Houben, J. D. Prades, V. Grillo, R. E. Dunin-Borkowski, J. R. Morante, A. Cabot, J. Arbiol, *ACS Nano* **2014**, *8*, 2290-2301; b) M. de la Mata, C. Magén, P. Caroff, J. Arbiol, *Nano Lett.* **2014**, *14*, 6614-6620; c) J. Arbiol, A. Cirera, F. Peiró, A. Cornet, J. R. Morante, J. J. Delgado, J. J. Calvino, *Appl. Phys. Lett.* **2002**, *80*, 329-331.
- [19] S. Farhadi, K. Pourzare, *Mater. Res. Bull.* **2012**, *47*, 1550-1556.
- [20] Z. W. Zhao, K. Konstantinov, L. Yuan, H. K. Liu, S. X. Dou, *J. Nanosci. Nanotechnol.* **2004**, *4*, 861-866.
- [21] G. X. Wang, X. P. Shen, J. Horvat, B. Wang, H. Liu, D. Wexler, J. Yao, *J. Phys. Chem. C* **2009**, *113*, 4357-4361.
- [22] a) X. M. He, X. Y. Song, W. Qiao, Z. W. Li, X. Zhang, S. M. Yan, W. Zhong, Y. W. Du, *J. Phys. Chem. C* **2015**, *119*, 9550-9559; b) X. M. He, W. Zhong, S. M. Yan, C. Liu, H. G. Shi, C. T. Au, Y. W. Du, *J. Phys. Chem. C* **2014**, *118*, 13898-13903.
- [23] M. R. Buck, A. J. Biacchi, R. E. Schaak, *Chem. Mater.* **2014**, *26*, 1492-1499.
- [24] a) J. F. Liu, S. Yin, H. P. Wu, Y. W. Zeng, X. R. Hu, Y. W. Wang, G. L. Lv, J. Z. Jiang, *J. Phys. Chem. B* **2006**, *110*, 21588-21592; b) W. S. Seo, J. H. Shim, S. J. Oh, E. K. Lee, N. H. Hur, J. T. Park, *J. Am. Chem. Soc.* **2005**, *127*, 6188-6189.
- [25] D. H. Lee, R. A. Condrate, *J. Mater. Sci.* **1999**, *34*, 139-146.
- [26] W. W. Yu, Y. A. Wang, X. G. Peng, *Chem. Mater.* **2003**, *15*, 4300-4308.
- [27] a) C. S. Lee, Z. F. Dai, S. Y. Jeong, C. H. Kwak, B. Y. Kim, D. H. Kim, H. W. Jang, J. S. Park, J. H. Lee, *Chem-Eur J* **2016**, *22*, 7102-7107; b) S. Wicker, K. Grossmann, N. Barsan, U. Weimar, *Sensor Actuat B-Chem* **2013**, *185*, 644-650.
- [28] a) J. M. Xu, J. Zhang, B. B. Wang, F. Liu, *J. Alloys Compd.* **2015**, *619*, 361-367; b) Z. Wen, L. P. Zhu, W. M. Mei, L. Hu, Y. G. Li, L. W. Sun, H. Cai, Z. Z. Ye, *Sensor Actuat B-Chem* **2013**, *186*, 172-179.

- [29] Q. Z. Jiao, M. Fu, C. You, Y. Zhao, H. S. Li, *Inorg. Chem.* **2012**, *51*, 11513-11520.
- [30] a) P. P. Zhang, J. W. Wang, X. X. Lv, H. Zhang, X. H. Sun, *Nanotechnology* **2015**, *26*; b) K.-I. Choi, H.-R. Kim, K.-M. Kim, D. Liu, G. Cao, J.-H. Lee, *Sensors and Actuators B: Chemical* **2010**, *146*, 183-189.